ENVIRONMENTAL SCIENCES

Air pollution–aerosol interactions produce more bioavailable iron for ocean ecosystems

Weijun Li,[1] Liang Xu,[1] Xiaohuan Liu,[2] Jianchao Zhang,[3] Yangting Lin,[3] Xiaohong Yao,[2] Huiwang Gao,[2] Daizhou Zhang,[4] Jianmin Chen,[1,5] Wenxing Wang,[1] Roy M. Harrison,[6,7] Xiaoye Zhang,[8] Longyi Shao,[9] Pingqing Fu,[10] Athanasios Nenes,[11,12,13,14] Zongbo Shi[6]*

It has long been hypothesized that acids formed from anthropogenic pollutants and natural emissions dissolve iron (Fe) in airborne particles, enhancing the supply of bioavailable Fe to the oceans. However, field observations have yet to provide indisputable evidence to confirm this hypothesis. Single-particle chemical analysis for hundreds of individual atmospheric particles collected over the East China Sea shows that Fe-rich particles from coal combustion and steel industries were coated with thick layers of sulfate after 1 to 2 days of atmospheric residence. The Fe in aged particles was present as a "hotspot" of (insoluble) iron oxides and throughout the acidic sulfate coating in the form of (soluble) Fe sulfate, which increases with degree of aging (thickness of coating). This provides the "smoking gun" for acid iron dissolution, because iron sulfate was not detected in the freshly emitted particles and there is no other source or mechanism of iron sulfate formation in the atmosphere.

INTRODUCTION

Iron (Fe) is a micronutrient that limits primary productivity in large areas of the surface ocean, particularly in high-nutrient, low-chlorophyll areas (*1*). Fe may also limit nitrogen (N) fixation in low-latitude, N-limited oceans (*2*, *3*). Soluble Fe from atmospheric deposition can stimulate primary production and/or nitrogen fixation in the surface ocean (*1*, *3*–*5*). Changes in the soluble Fe input to the oceans could have an important impact on oceanic carbon uptake and storage and indirectly affect the climate (*6*).

Recent modeling studies have suggested that anthropogenic activities may have led to a doubling or even tripling of atmospheric soluble Fe deposition to the oceans since the Industrial Revolution (*6*–*11*). If confirmed, this increase in soluble Fe could have a major impact on ocean productivity, carbon uptake, ocean oxygen depletion and associated biogeochemical feedback, and climate (*6*, *11*). A key component of these models is the hypothesized "Fe acid dissolution" process: Acids formed from anthropogenic gaseous pollutants such as sulfur dioxide dissolve iron in aerosol particles (*12*–*14*), making them bioavailable and increasing the bioavailable iron input to the oceans. Because of the potential importance of this process in the Fe cycle and ocean biogeochemistry, a number of field and laboratory studies have been carried out to test this hypothesis in the last decade. Laboratory studies found a positive relationship between Fe solubility (soluble Fe–to–total Fe ratio) and aerosol acidity (*8*, *14*–*16*), providing indirect support to the hypothesis. However, field observations have been less conclusive (*17*–*19*). A key limitation is that previous studies have been based on bulk aerosol analysis and do not provide information on the distribution of soluble Fe in individual aerosol particles and how it relates to acidic compounds on a per-particle basis (*20*). Oakes *et al.* (*21*) showed, using bulk aerosol analysis upon ambient particle samples, that soluble Fe was correlated with sulfate in aerosol, a relationship consistent with low-pH environments. Longo *et al.* (*22*) recently suggested, through a combination of bulk measurements and some Fe mineral speciation with x-ray absorption near-edge structure, that strong acidity likely contributes to higher aerosol Fe solubility. Recently, Rindelaub *et al.* (*23*) demonstrated the potential of Raman microspectroscopy in measuring the pH in individual particles, but challenges in its application to atmospheric particles remain. The limitation of bulk analysis and the difficulty of measuring Fe species in individual aerosol particles (*23*, *24*) make it highly challenging to test the Fe acid dissolution hypothesis.

RESULTS AND DISCUSSION

We used novel individual particle analysis techniques including nanoscale secondary ion mass spectrometry (NanoSIMS) and scanning transmission electron microscopy (STEM) to provide indisputable evidence of the Fe dissolution process from acids deposited on atmospheric particles. We collected a number of aerosol samples during a research cruise over the Yellow Sea in June 2013 (fig. S1A). Back trajectory analyses (fig. S2) indicated that air masses reaching the sampling sites were chiefly from mainland China. We investigated the composition and sources of Fe-bearing particles in the collected aerosol samples. The sizes of the particles were measured on the basis of projected area on microscopic photographs and then corrected to volume-based diameters (fig. S3). The chemical composition of 5511 particles with a size range of 20 to 5000 nm was analyzed using a transmission electron microscope (TEM) with an energy-dispersive x-ray spectrometer (EDS). Fe was detected in 14% (ranging from 5 to 29%) of all analyzed particles.

[1]Environment Research Institute, Shandong University, Jinan, Shandong 250100, China. [2]Key Laboratory of Marine Environment and Ecology, Ministry of Education, Ocean University of China, Qingdao 266100, China. [3]Key Laboratory of Earth and Planetary Physics, Institute of Geology and Geophysics, Chinese Academy of Sciences, Beijing 100029, China. [4]Faculty of Environmental and Symbiotic Sciences, Prefectural University of Kumamoto, Kumamoto 862-8502, Japan. [5]Shanghai Key Laboratory of Atmospheric Particle Pollution and Prevention, Department of Environmental Science and Engineering, Fudan University, Shanghai 200433, China. [6]School of Geography, Earth and Environmental Sciences, University of Birmingham, Birmingham, U.K. [7]Department of Environmental Sciences, Center of Excellence in Environmental Studies, King Abdulaziz University, P. O. Box 80203, Jeddah 21589, Saudi Arabia. [8]Key Laboratory of Atmospheric Chemistry, Chinese Academy of Meteorological Sciences, Beijing, China. [9]State Key Laboratory of Coal Resources and Safe Mining, China University of Mining and Technology, Beijing 100086, China. [10]State Key Laboratory of Atmospheric Boundary Layer Physics and Atmospheric Chemistry, Institute of Atmospheric Physics, Chinese Academy of Sciences, Beijing 100029, China. [11]School of Earth and Atmospheric Sciences, Georgia Institute of Technology, Atlanta, GA 30332, USA. [12]School of Chemical and Biomolecular Engineering, Georgia Institute of Technology, Atlanta, GA 30332, USA. [13]Institute of Chemical Engineering Sciences, Foundation for Research and Technology Hellas, Patras GR-26504, Greece. [14]Institute for Environmental Research and Sustainable Development, National Observatory of Athens, Palea-Pendeli GR-15236, Greece.
*Corresponding author. Email: z.shi@bham.ac.uk

We observed three main types of Fe-bearing particles: Fe-rich (Fig. 1A and fig. S4A), fly ash (Fig. 1B), and mineral dust. Fe-rich particles are distinct from coal fly ash particles: Fe in the former is the major element in their EDS spectra (for example, top EDS spectrum in Fig. 1), while that in the latter is a minor element (for example, bottom EDS spectrum in Fig. 1). Fly ash and Fe-rich particles were darker (more electron-dense) than secondary sulfate or organic matter (OM) under the TEM (Fig. 1, A and B). Fe-rich particles and fly ash usually displayed a spherical shape (Fig. 1, A and B), with the former mainly containing Fe and the latter containing Si, Al, and Fe (Fig. 1B). Mineral dust particles usually displayed an irregular shape and contained Si and Al with a small amount of Fe.

Fe-bearing particles were classified as externally mixed particles (that is, primary Fe-rich, fly ash, or mineral dust) and internally mixed particles (that is, primary particles mixed with sulfate and OM) (fig. S5). The contribution of externally mixed fly ash and Fe-rich particles to total Fe-bearing particles decreased from 64% for particles with a diameter of 20 to 200 nm, to 20% for particles with a diameter of 200 to 400 nm, to less than 5% for those with a diameter of >400 nm (Fig. 2). Overall, 75% of the Fe-bearing particles were internal mixtures of Fe-rich/fly ash and sulfate (Fig. 2).

STEM elemental maps show that Fe was distributed throughout the entire particle, in addition to the Fe hotpots (for example, see Fig. 3, A and B). The spherical morphology of Fe-rich or fly ash particles (Figs. 1 and 3A) suggests that they were formed via high-temperature processes followed by a fast cooling process (*25*). They were primarily emitted from anthropogenic emissions, such as coal combustion or industrial processes.

No sulfur was detected in Fe-rich particles collected from a steelworks or in coal fly ash particles collected from a power plant using TEM-EDS (fig. S6, A and B). However, most of the fly ash and Fe-rich particles collected over the Yellow Sea contained a significant amount of sulfate. More than 80% of the Fe-bearing particles larger than 200 nm were coated with sulfate (marked as "Sulfate with Fe inclusions" in Fig. 2), suggesting that the sulfate was formed in the atmosphere via gas-to-particle conversion. Almost none of the analyzed individual particles showed evidence of sodium, suggesting that the S is not associated with sea salt. Because most SO_2 in East Asia is emitted from power plants and industries (*26*, *27*), and most of the sulfate aerosol is formed from anthropogenic SO_2 in the Northern Hemisphere (*28*), we argue that the sulfate aerosol found in the individual aerosol particles is primarily formed from anthropogenic SO_2.

The overall size of Fe-bearing particles ranges from 20 nm to 5 μm, with a peak at 700 nm; the size of Fe-rich/fly ash grains within these particles are much smaller, ranging from 20 nm to 1 μm, with a peak at 160 nm (fig. S7). On average, the size of the primary particles (that is, Fe-rich particles or fly ash) increased fourfold after 1 to 2 days of transport. This suggests that secondary aerosol formation on the Fe-rich/fly ash particles is very efficient, possibly involving trace metal or acid-catalyzed reactions in aqueous aerosol (*29*, *30*).

STEM elemental maps showed an overlap of elemental Fe and S in most of the analyzed Fe-bearing particles, in addition to that in the Fe hotspots (for example, see Fig. 3, A and B). This suggests that the Fe dispersed in the secondary coating is released from the Fe-rich or fly ash inclusions, because there is no vapor-phase Fe in the atmosphere. In addition, if this Fe was present as insoluble Fe, such as Fe oxides or aluminosilicate, it would have only existed as individual grains, that is, nanoparticles. However, this is not the case, suggesting that the Fe in the secondary coating is likely to be present as soluble Fe, such as Fe sulfate.

We confirmed the presence of Fe sulfate in the sulfate coatings by NanoSIMS analysis of individual particles in the same samples. Figure 3C shows an example of ion intensity maps of CN^-, FeO^-, S^-, and FeS^- in an individual particle: The particle has two FeO^- hotspots, with FeS^- distributed in the S^- matrix. The FeO^- hotspots are likely from Fe oxides or fly ash inclusions, similar to those shown in standard samples (fig. S8A), whereas the FeS^- signal is from Fe sulfate (fig. S8B). Furthermore, the acid dissolution process reproduced in the laboratory showed a distribution pattern for FeS^-, FeO^-, and S^- signals in NanoSIMS ion

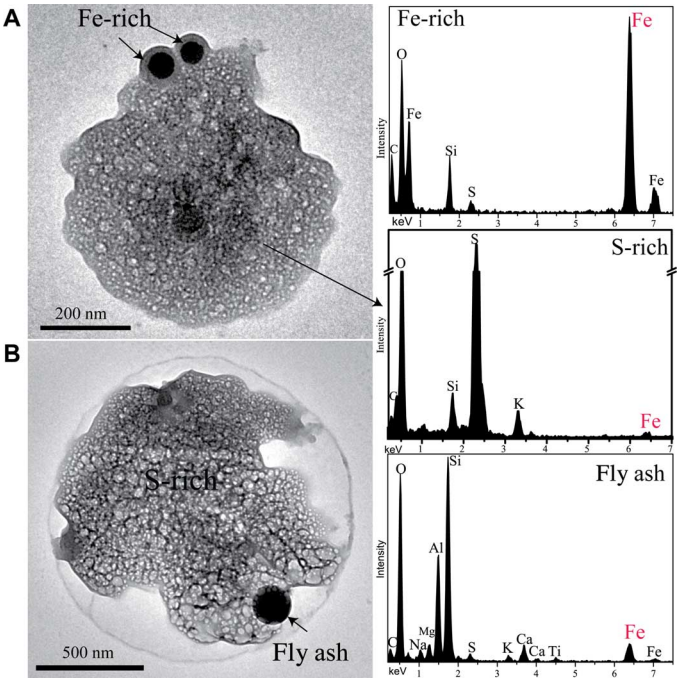

Fig. 1. TEM images and EDS spectra of two typical Fe-bearing particles collected over the Yellow Sea. (**A**) Two spherical Fe-rich particles internally mixed with sulfate. (**B**) A spherical fly ash particle internally mixed with sulfate.

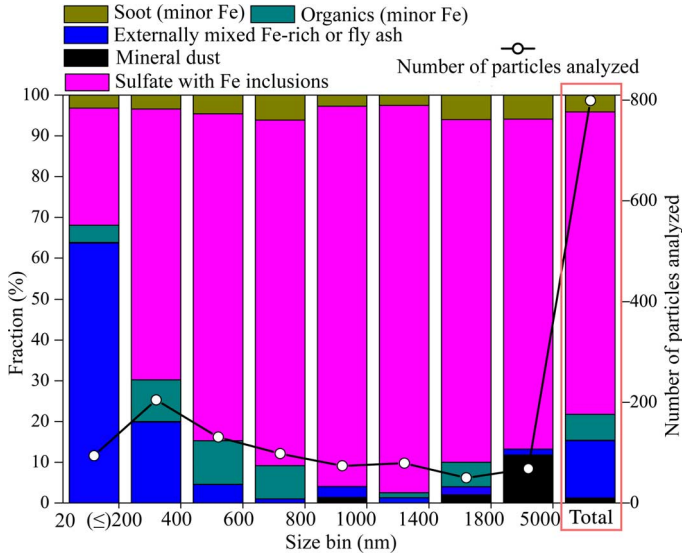

Fig. 2. Number fraction of different types of Fe-bearing aerosols at different size ranges.

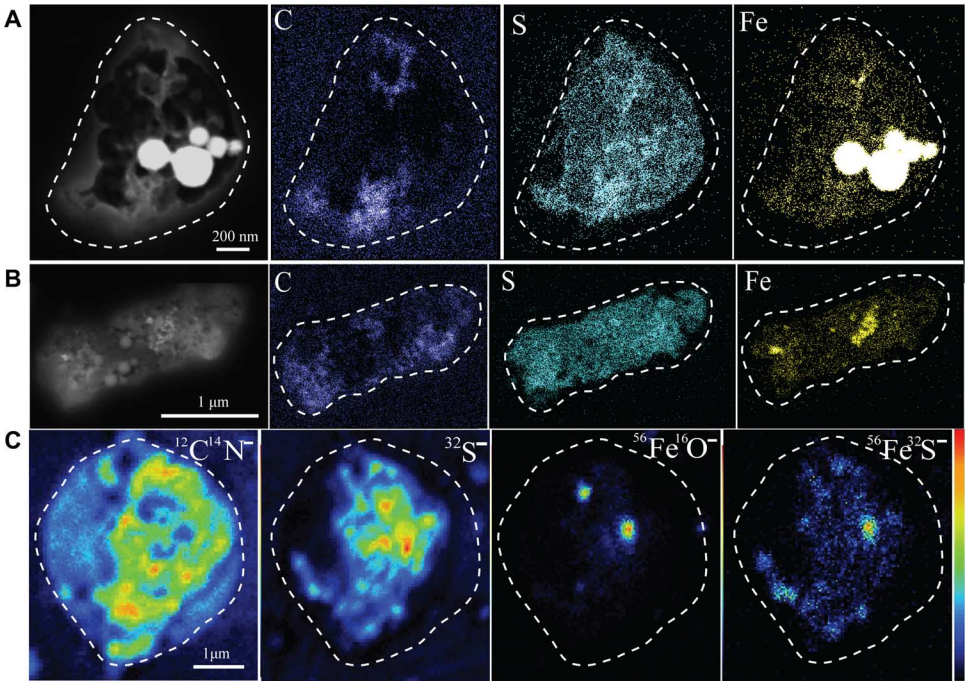

Fig. 3. Dark-field TEM images and elemental maps of C, S, and Fe and NanoSIMS ion intensity maps of CN^-, S^-, FeO^-, and FeS^- of an individual Fe-bearing particle. (**A** and **B**) Elemental maps showing two individual sulfate particles with Fe-rich particles (as hotspots). (**C**) Ion intensity maps showing the presence of OM, sulfate, Fe oxide, and Fe sulfate.

maps as well as for Fe and S elemental maps (figs. S8C and S9) that is similar to that of the real atmospheric particles (Fig. 3 and fig. S10). These results demonstrated that at least part of the Fe in the sulfate coating of ambient particles is present as Fe sulfate, which can only be formed from primary Fe particles (for example, fly ash or Fe-rich particles).

To further demonstrate the environmental relevance of the above-mentioned results, we carried out NanoSIMS measurements of ion intensity maps in a number of individual particles collected during the cruise. We then plotted the $FeS^-/(FeS^- + FeO^-)$ ratio against the $S^-/(FeS^- + FeO^-)$ ratio in Fig. 4. The former is an indicator of solubility, while the latter reflects the thickness of sulfate coating relative to total Fe. Figure 4 shows that $FeS^-/(FeS^- + FeO^-)$ ratio increased with the $S^-/(FeS^- + FeO^-)$ ratio. Moreover, selected-area electron diffraction (SAED) confirmed that the sulfate coating in the randomly selected individual particles is more likely to be (acidic) ammonium bisulfate (fig. S4). This finding provides further support for higher solubility in individual particles associated with sulfate availability (in proportion to the total Fe present in the particles), an indicator of acidity in an ammonia-poor atmosphere (*31*), particularly at higher altitudes. Particles generated from a filtered water leach of an urban $PM_{2.5}$ (particulate matter with an aerodynamic diameter of less than 2.5 μm) sample collected during a haze event in the North China Plain produced a medium $FeS^-/(FeO^-+FeS^-)$ ratio that is close to the regression line (Fig. 4). Because haze particles in China are predominantly secondary in origin (*32*), the acidic aqueous phase contained within the haze provides the necessary medium for acid dissolution.

A potential contradiction to the inferred acid dissolution process is that some of the Fe in the sulfate coating may be directly released from the soluble Fe on the surface of the primary Fe-rich or fly ash particles. However, this possibility is unlikely because no Fe was detected in the sulfate coating around coal fly ash generated from the suspension of

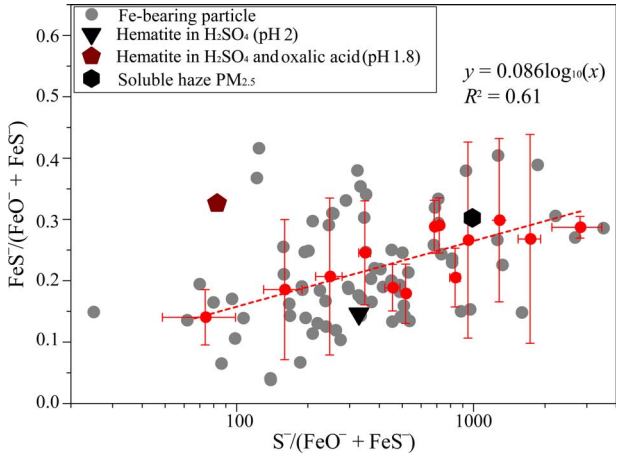

Fig. 4. Relationship between $S^-/(FeS^- + FeO^-)$ and $FeS^-/(FeO^- + FeS^-)$ in individual aerosol particles. These include 84 Fe-bearing particles from the East China Sea, three laboratory-generated aerosol samples [hematite in H_2SO_4 (pH 2) (triangle), hematite in H_2SO_4 (pH 1.8) with oxalate (pentagon), and soluble fraction of haze $PM_{2.5}$ (hexagon)]. The red dots represent the average values of $S^-/(FeS^- + FeO^-)$ versus $FeS^-/(FeO^- + FeS^-)$ from all Fe-bearing particles over different size ranges (<100, 200, 300, 400, 500, 600, 700, 800, 900, 1000, 1500, 2000, and 3600 nm), whereas the red line shows the regression of average $FeS^-/(FeO^- + FeS^-)$ and logometric values of average $S^-/(FeO^- + FeS^-)$. Error bars represent the degree of data dispersion within different size ranges.

coal fly ash in nonacidic ammonium sulfate solution (figs. S6C and S11; see experiment 3). This is consistent with the results of a previous study in which the initial solubility of Fe measured in coal fly ash is very low (much less than 1%) (*16*). Fe-rich particles from the iron/steel industry are also unlikely to be soluble in water because they are mainly

composed of Fe oxides (for example, magnetite in fig. S4). Although Fe particles from ship and vehicle emissions or biomass burning may be highly soluble (for example, >50%) (*21*, *33*), their contribution to all Fe-bearing particles is very small. In summary, the detection of Fe sulfate, mixed within the sulfate coatings, provides the "smoking gun" for acid dissolution—because there is no other atmospheric source of Fe sulfate or process that leads to its formation.

Our work also indirectly confirms the presence of the aerosol acidification process in the atmosphere. Although thermodynamic models, ion balance, or phase partitioning often predicts high acidity in wet aerosols (*12*, *13*, *31*, *34*–*36*), aerosol acidity in individual particles has never been measured because of the technological challenges in measuring pH in the miniscule amounts of water associated with aerosol particles (*23*, *24*). Our results confirm the existence of an acid dissolution process, providing indirect evidence that the aerosols become acidic after transport to the Yellow Sea. This is further supported by the SAED measurement, which showed that S is present as acidic ammonium bisulfate in the analyzed individual particles (fig. S4). Recently, Wang *et al.* (*37*) argued that acids in aerosols in two Chinese megacities are completely neutralized by ammonium but we showed that aerosols in the Asian outflow is acidic. Future work needs to determine the spatial and temporal variability of aerosol acidity across size.

Current Fe emission inventories indicate that coal fly ash and dust globally contributed 0.45 and 7.8 Tg of total Fe per year deposited to the oceans (*38*). Ito and Shi (*8*) simulated the atmospheric acid Fe dissolution processes and calculated that the Fe solubility at deposition is ca. 8% for coal fly ash in the present day and ca. 0.27% for dust in the preindustrial era. Using these estimates, we calculated that soluble Fe deposition to the ocean from coal fly ash alone may be 50% more than that from natural dust. Acid dissolution of Fe in particles from the steel industry (*38*) and deserts (*7*–*12*, *35*, *36*) due to anthropogenic acidic gas emissions will certainly add more soluble Fe to the oceans. Thus, the Fe acid dissolution process associated with anthropogenic gas emissions may have significantly enhanced the soluble Fe deposition to the ocean. Mahowald *et al.* (*6*) estimated that even a doubling in soluble Fe deposition to the oceans could have resulted in a 6% increase in ocean productivity and an additional 8 Pg of carbon drawdown. Furthermore, Ito *et al.* (*11*) showed that the impact of increased soluble Fe supply to the oceans on productivity and carbon export may have contributed to the observed expansion of the oxygen depletion in many regions of the world with important impacts on ecosystems and biogeochemical cycles. It is also important to note that soluble Fe from anthropogenic aerosols (for example, coal fly ash) may have a disproportionately larger impact on marine ecosystems than dust—because they tend to deposit to the Fe-limited ecosystems (*1*, *2*, *39*) and their emissions are continuous throughout the year, in contrast to those of the dust (*9*, *31*, *38*–*40*). Looking into the future, changes in acidic gas emissions from natural or anthropogenic processes and atmospheric acidity will affect this Fe dissolution process and thus the soluble Fe to the oceans. Therefore, it is essential that Earth system models capture this process to better understand the interaction of air pollution with the atmospheric Fe cycle and ocean biogeochemistry (*6*, *11*).

MATERIALS AND METHODS

Sample collection

Eighteen atmospheric particle samples were collected during a research cruise (*Dongfanghong 2*) over the Yellow Sea (fig. S1A) from 23 to 30 June 2013. The Yellow Sea is located between mainland China and the Korean Peninsula and is the northern part of the East China Sea, a marginal sea of the Pacific Ocean. All aerosol samples were collected onto copper TEM grids coated with carbon film (carbon type-B, 300-mesh copper; Tianld Co.) using a single-stage cascade impactor. Sampling durations varied from 10 to 15 min depending on particle loading to avoid particle aggregation during sample collection. Each sample was placed in a sealed dry plastic tube and stored in a desiccator at 25°C and 20 ± 3% relative humidity to minimize exposure to ambient air until further analysis. The red dots on the cruise track indicated where the samples were collected (fig. S1).

Aerosol optical depths (AODs) at 550 nm from the MODIS Terra sensor (data product: MODIS-Terra ver. 5.1) were obtained through the online Giovanni interface (*41*). The regional AOD distribution from 20 to 30 June 2013 suggests a gradient of high to low AOD from mainland China to the Yellow Sea (fig. S1B). Air mass back trajectory analysis indicates that most of the air masses reaching the cruise passed over the polluted coastal cities of East China (fig. S2).

Laboratory standard sample preparation

We have prepared a series of standards to verify our field results. Coal fly ash and Fe-rich particle samples were collected from the hoppers of electrostatic precipitators of a coal-fired power plant and a steelworks, respectively, in Linyi City, Shandong. Hematite, as an Fe oxide standard, was purchased from Sinopharm Chemical Reagent Co. Ltd. Four types of additional "standard" samples were prepared:

Experiment 1. Hematite and sulfuric acid: 2.5 mg of hematite powder was added to diluted sulfuric acid to a final pH of 2.0. This experiment was carried out to simulate the acidic processing of Fe oxides, similar to previous studies (*14*–*16*, *42*–*50*).

Experiment 2. Hematite and sulfuric + oxalic acid: 15.7 mg of hematite and 22.5 mg of $H_2C_2O_4$ powders (Sigma-Aldrich) were added to dilute sulfuric H_2SO_4 to a final pH value of 1.8. This experiment aimed to simulate the acid and oxalate processing of Fe oxides (*8*, *51*).

Experiment 3. Coal fly ash in a near-neutral ammonium sulfate solution: 5.0 mg of coal fly ash was added to $(NH_4)_2SO_4$ solution (0.1 M) (pH 5.6). This experiment was used to test whether there is soluble Fe in untreated coal fly ash.

Experiment 4. Haze particle leach: A $PM_{2.5}$ sample was collected onto a Teflon filter during a haze event in Jinan (in the North China Plain); the sample was leached with 10 ml of Milli-Q water and then filtered using a membrane filter with a pore size of 0.2 μm.

Suspensions from Exps. 1 to 3 were shaken for 24 hours at room temperature before further processing. The water leach of the $PM_{2.5}$ sample was prepared immediately before aerosol atomization. Aerosol particles were then generated from the particle suspensions (Exps. 1 to 3) and the filtrate (experiment 4) using an atomizer (Badger Airbrushes 150-7) and collected onto TEM grids.

Offline microscopic and spectroscopic analysis

Aerosol and standard particles collected on TEM grids were analyzed with a JEOL JEM-2100 TEM operated at 200 kV. To ensure that the analyzed particles were representative of the ambient sample, five areas were chosen from the center and periphery of the sampling spot on each grid. Every particle in the selected area was analyzed using EDS. EDS spectra were collected for 30 s to minimize radiation exposure and potential beam damage (*52*). Chemical composition of a total of 5511 individual particles ranging from 20 to 5000 nm was recorded. The area of an individual particle or the inclusion therein was

measured by using the iTEM system, on the basis of which the equivalent area diameter (EAD) was calculated (*53*). The SAED and fast Fourier diffraction patterns derived from crystal lattice spacings were used to confirm the phases of minerals in individual particles.

To correct the EAD to volume-based equivalent spherical diameters (ESDs), we obtained the two- and three-dimensional images of airborne particles using a Digital Nanoscope IIIa atomic force microscope (AFM) (*54*, *55*). The instrument was operated in tapping mode with a cantilever and conical tip with a radius of 10 nm for imaging. Usually, particle images were taken at a full scan size of 10 μm, which included 10 to 15 particles. By comparing the ESD and EAD of the same particles, we observed a linear relationship between the two parameters (fig. S3), which was used to convert EAD measured under iTEM into ESD (fig. S7).

On the basis of the TEM analysis, we chose four typical aerosol samples for STEM analysis using a JEOL 2100F field-emission TEM equipped with an Oxford EDS system. STEM provides high-resolution elemental mapping (*53*, *56*). These four samples were further analyzed by NanoSIMS 50L (Institute of Geology and Geophysics, Chinese Academy of Sciences). NanoSIMS can provide high-resolution chemical mapping (*54*, *57*). The instrument was set to simultaneous secondary ion collection mode with pulse counting on electron multipliers, enabling us to simultaneously collect seven secondary ions originating from the same sputtered volume of the sample. A microcesium source was used to generate Cs^+ primary ions, with an impact energy of 16 kV for sample interrogation. $Fe_2(SO_4)_3$ powder was used to calibrate peaks (mass/charge ratio values) of $^{32}S^-$, $^{56}Fe^{16}O^-$, and $^{56}Fe^{32}S^-$ (fig. S8). Because the substrate of TEM grid is carbon, $^{12}C^{14}N^-$ is used to represent OM in individual particles, whereas $^{32}S^-$ is used for secondary sulfate (*58*, *59*). Ion clusters of $^{56}Fe^{16}O^-$ can be generated from hematite (fig. S8A) as well as Fe sulfates in individual particles (fig. S8B), whereas $^{56}Fe^{16}S^-$ can only be generated from Fe sulfate particles (fig. S8B). No $^{56}Fe^{16}S^-$ ion was detected in the hematite standard (fig. S8A).

SUPPLEMENTARY MATERIALS

Supplementary material for this article is available at http://advances.sciencemag.org/cgi/content/full/3/3/e1601749/DC1

fig. S1. Cruise route and AOD map.
fig. S2. Air mass back trajectories at 1500 m of each sampling station over the Yellow Sea.
fig. S3. The correlation of ESD and EAD based on AFM analysis.
fig. S4. TEM micrographs of an Fe-rich particle and a sulfate particle collected over the East China Sea.
fig. S5. Morphology and mixing state of Fe-rich and fly ash particles.
fig. S6. TEM image of Fe-rich and coal fly ash particles collected at sources.
fig. S7. Size distributions of Fe-rich and fly ash inclusions only and Fe-bearing particles.
fig. S8. NanoSIMS ion intensity of S^-, FeO^-, and FeS^- in standard samples.
fig. S9. Dark-field image and elemental mapping of an individual hematite-bearing particle (experiment 1).
fig. S10. NanoSIMS ion intensity of C^-, CN^-, S^-, FeO^-, and FeS^- in individual particles collected over the Yellow Sea.
fig. S11. Dark-field image and elemental mapping of an internally mixed particle generated from ammonium sulfate solution (pH 5.6) mixed with coal fly ash.

REFERENCES AND NOTES

1. J. H. Martin, J. H. Martin, K. H. Coale, K. S. Johnson, S. E. Fitzwater, R. M. Gordon, S. J. Tanner, C. N. Hunter, V. A. Elrod, J. L. Nowicki, T. L. Coley, R. T. Barber, S. Lindley, A. J. Watson, K. Van Scoy, C. S. Law, M. I. Liddicoat, R. Ling, T. Stanton, J. Stockel, C. Collins, A. Anderson, R. Bidigare, M. Ondrusek, M. Latasa, F. J. Millerostar, K. Leestar, W. Yao, J. Z. Zhangstar, G. Friederich, C. Sakamoto, F. Chavez, K. Buck, Z. Kolber, R. Greene, P. Falkowski, S. W. Chisholm, F. Hoge, R. Swift, J. Yungel, S. Turner, P. Nightingale, A. Hatton, P. Liss, N. W. Tindale, Testing the iron hypothesis in ecosystems of the equatorial Pacific Ocean. *Nature* **371**, 123–129 (1994).
2. C. M. Moore, M. M. Mills, K. R. Arrigo, I. Berman-Frank, L. Bopp, P. W. Boyd, E. D. Galbraith, R. J. Geider, C. Guieu, S. L. Jaccard, T. D. Jickells, J. La Roche, T. M. Lenton, N. M. Mahowald, E. Marañón, I. Marinov, J. K. Moore, T. Nakatsuka, A. Oschlies, M. A. Saito, T. F. Thingstad, A. Tsuda, O. Ulloa, Processes and patterns of oceanic nutrient limitation. *Nat. Geosci.* **6**, 701–710 (2013).
3. T. Jickells, C. M. Moore, The importance of atmospheric deposition for ocean productivity. *Annu. Rev. Ecol. Evol. Syst.* **46**, 481–501 (2015).
4. C. Schlosser, J. K. Kla, B. D. Wake, J. T. Snow, D. J. Honey, E. M. S. Woodward, M. C. Lohan, E. P. Achterberg, C. M. Moore, Seasonal ITCZ migration dynamically controls the location of the (sub)tropical Atlantic biogeochemical divide. *Proc. Natl. Acad. Sci. U.S.A.* **111**, 1438–1442 (2014).
5. C. S. Law, E. Breviere, G. de Leeuw, V. Garcon, C. Guieu, D. J. Kieber, S. Kontradowitz, A. Paulmier, P. K. Quinn, E. S. Saltzman, J. Stefels, R. von Glasow, Evolving research directions in Surface Ocean–Lower Atmosphere (SOLAS) science. *Environ. Chem.* **10**, 1–16 (2013).
6. N. M. Mahowald, S. Kloster, S. Engelstaedter, J. K. Moore, S. Mukhopadhyay, J. R. McConnell, S. Albani, S. C. Doney, A. Bhattacharya, M. A. J. Curran, M. G. Flanner, F. M. Hoffman, D. M. Lawrence, K. Lindsay, P. A. Mayewski, J. Neff, D. Rothenberg, E. Thomas, P. E. Thornton, C. S. Zender, Observed 20th century desert dust variability: Impact on climate and biogeochemistry. *Atmos. Chem. Phys.* **10**, 10875–10893 (2010).
7. A. Ito, Atmospheric processing of combustion aerosols as a source of bioavailable iron. *Environ. Sci. Technol. Lett.* **2**, 70–75 (2015).
8. A. Ito, Z. Shi, Delivery of anthropogenic bioavailable iron from mineral dust and combustion aerosols to the ocean. *Atmos. Chem. Phys.* **16**, 85–99 (2016).
9. C. Luo, N. Mahowald, T. Bond, P. Y. Chuang, P. Artaxo, R. Siefert, Y. Chen, J. Schauer, Combustion iron distribution and deposition. *Global Biogeochem. Cycles* **22**, GB1012 (2008).
10. S. Myriokefalitakis, N. Daskalakis, N. Mihalopoulos, A. Baker, A. Nenes, M. Kanakidou, Changes in dissolved iron deposition to the oceans driven by human activity: A 3-D global modelling study. *Biogeosciences* **12**, 3973–3992 (2015).
11. T. Ito, A. Nenes, M. S. Johnson, N. Meskhidze, C. Deutsch, Acceleration of oxygen decline in the tropical Pacific over the past decades by aerosol pollutants. *Nat. Geosci.* **9**, 443–447 (2016).
12. N. Meskhidze, W. L. Chameides, A. Nenes, G. Chen, Iron mobilization in mineral dust: Can anthropogenic SO_2 emissions affect ocean productivity? *Geophys. Res. Lett.* **30**, 2085 (2003).
13. X. Zhu, J. M. Prospero, F. J. Millero, D. L. Savoie, G. W. Brass, The solubility of ferric ion in marine mineral aerosol solutions at ambient relative humidities. *Mar. Chem.* **38**, 91–107 (1992).
14. L. J. Spokes, T. D. Jickells, Factors controlling the solubility of aerosol trace metals in the atmosphere and on mixing into seawater. *Aquat. Geochem.* **1**, 355–374 (1995).
15. Z. Shi, M. D. Krom, T. D. Jickells, S. Bonneville, K. S. Carslaw, N. Mihalopoulos, A. R. Baker, L. G. Benning, Impacts on iron solubility in the mineral dust by processes in the source region and the atmosphere: A review. *Aeolian Res.* **5**, 21–42 (2012).
16. H. Chen, A. Laskin, J. Baltrusaitis, C. A. Gorski, M. M. Scherer, V. H. Grassian, Coal fly ash as a source of iron in atmospheric dust. *Environ. Sci. Technol.* **46**, 2112–2120 (2012).
17. A. R. Baker, T. D. Jickells, M. Witt, K. L. Linge, Trends in the solubility of iron, aluminium, manganese and phosphorus in aerosol collected over the Atlantic Ocean. *Mar. Chem.* **98**, 43–58 (2006).
18. C. S. Buck, W. M. Landing, J. A. Resing, C. I. Measures, The solubility and deposition of aerosol Fe and other trace elements in the North Atlantic Ocean: Observations from the A16N CLIVAR/CO_2 repeat hydrography section. *Mar. Chem.* **120**, 57–70 (2010).
19. C. S. Buck, W. M. Landing, J. Resing, Pacific Ocean aerosols: Deposition and solubility of iron, aluminum, and other trace elements. *Mar. Chem.* **157**, 117–130 (2013).
20. A. R. Baker, P. L. Croot, Atmospheric and marine controls on aerosol iron solubility in seawater. *Mar. Chem.* **120**, 4–13 (2010).
21. M. Oakes, E. D. Ingall, B. Lai, M. M. Shafer, M. D. Hays, Z. G. Liu, A. G. Russell, R. J. Weber, Iron solubility related to oarticle sulfur content in source emission and ambient fine particles. *Environ. Sci. Technol.* **46**, 6637–6644 (2012).
22. F. Longo, Y. Feng, B. Lai, W. M. Landing, R. U. Shelley, A. Nenes, N. Mihalopoulos, K. Violaki, E. D. Ingall, Influence of atmospheric processes on the solubility and composition of iron in saharan dust. *Environ. Sci. Technol.* **50**, 6912–6920 (2016).
23. J. D. Rindelaub, R. L. Craig, L. Nandy, A. L. Bondy, C. S. Dutcher, P. B. Shepson, A. P. Ault, Direct measurement of pH in individual particles via raman microspectroscopy and variation in acidity with relative humidity. *J. Phys. Chem. A* **120**, 911–917 (2016).
24. J. Hennigan, J. Izumi, A. P. Sullivan, R. J. Weber, A. Nenes, A critical evaluation of proxy methods used to estimate the acidity of atmospheric particles. *Atmos. Chem. Phys. Discuss.* **15**, 2775–2790 (2015).
25. Y. Chen, N. Shah, F. E. Huggins, G. P. Huffman, Transmission electron microscopy investigation of ultrafine coal fly ash oarticles. *Environ. Sci. Technol.* **39**, 1144–1151 (2005).
26. Q. Zhang, D. Streets, G. Carmichael, K. B. He, H. Huo, A. Kannari, Z. Klimont, I. S. Park, S. Reddy, J. S. Fu, D. Chen, L. Duan, Y. Lei, L. T. Wang, Z. L. Yao, Asian emissions in 2006 for the NASA INTEX-B mission. *Atmos. Chem. Phys.* **9**, 5131–5153 (2009).

27. Z. Lu, D. G. Streets, Q. Zhang, S. Wang, G. R. Carmichael, Y. F. Cheng, C. Wei, M. Chin, T. Diehl, Q. Tan, Sulfur dioxide emissions in China and sulfur trends in East Asia since 2000. *Atmos. Chem. Phys.* **10**, 6311–6331 (2010).
28. J. Liu, D. L. Mauzerall, L. W. Horowitz, Source-receptor relationships between East Asian sulfur dioxide emissions and Northern Hemisphere sulfate concentrations. *Atmos. Chem. Phys. Discuss.* **8**, 5537–5561 (2008).
29. H. He, Y. Wang, Q. Ma, J. Ma, B. Chu, D. Ji, G. Tang, C. Liu, H. Zhang, J. Hao, Mineral dust and NOx promote the conversion of SO_2 to sulfate in heavy pollution days. *Sci. Rep.* **4**, 4172 (2014).
30. E. Harris, B. Sinha, D. van Pinxteren, A. Tilgner, K. Wadinga Fomba, J. Schneider, A. Roth, T. Gnauk, B. Fahlbusch, S. Mertes, T. Lee, J. Collett, S. Foley, S. Borrmann, P. Hoppe, H. Herrmann, Enhanced role of transition metal ion catalysis during in-cloud oxidation of SO_2. *Science* **340**, 727–730 (2013).
31. A. Bougiatioti, P. Nikolaou, I. Stavroulas, G. Kouvarakis, R. Weber, A. Nenes, M. Kanakidou, N. Mihalopoulos, Particle water and pH in the eastern Mediterranean: Source variability and implications for nutrient availability. *Atmos. Chem. Phys.* **16**, 4579–4591 (2016).
32. S. Guo, M. Hu, M. L. Zamora, J. Peng, D. Shang, J. Zheng, Z. Du, Z. Wu, M. Shao, L. Zeng, M. J. Molina, R. Zhang, Elucidating severe urban haze formation in China. *Proc. Natl. Acad. Sci. U.S.A.* **111**, 17373–17378 (2014).
33. A. W. Schroth, J. Crusius, E. R. Sholkovitz, B. C. Bostick, Iron solubility driven by speciation in dust sources to the ocean. *Nat. Geosci.* **2**, 337–340 (2009).
34. R. J. Weber, H. Guo, A. G. Russell, A. Nenes, High aerosol acidity despite declining atmospheric sulfate concentrations over the past 15 years. *Nat. Geosci.* **9**, 282–285 (2016).
35. N. Meskhidze, W. L. Chameides, A. Nenes, Dust and pollution: A recipe for enhanced ocean fertilization? *J. Geophys. Res.* **110**, D03301 (2005).
36. F. Solmon, P. Y. Chuang, N. Meskhidze, Y. Chen, Acidic processing of mineral dust iron by anthropogenic compounds over the north Pacific Ocean. *J. Geophys. Res.* **114**, D02305 (2009).
37. G. Wang, R. Zhang, M. E. Gomez, L. Yang, M. Levy Zamora, M. Hu, Y. Lin, J. Peng, S. Guo, J. Meng, J. Li, C. Cheng, T. Hu, Y. Ren, Y. Wang, J. Gao, J. Cao, Z. An, W. Zhou, G. Li, J. Wang, P. Tian, W. Marrero-Ortiz, J. Secrest, Z. Du, J. Zheng, D. Shang, L. Zeng, M. Shao, W. Wang, Y. Huang, Y. Wang, Y. Zhu, Y. Li, J. Hu, B. Pan, L. Cai, Y. Cheng, Y. Ji, F. Zhang, D. Rosenfeld, P. S. Liss, R. A. Duce, C. E. Kolb, M. J. Molina, Persistent sulfate formation from London Fog to Chinese haze. *Proc. Natl. Acad. Sci. U.S.A.* **113**, 13630–13635 (2016).
38. R. Wang, Y. Balkanski, O. Boucher, L. Bopp, A. Chappell, P. Ciais, D. Hauglustaine, J. Peñuelas, S. Tao, Sources, transport and deposition of iron in the global atmosphere. *Atmos. Chem. Phys.* **15**, 6247–6270 (2015).
39. A. Ito, Global modeling study of potentially bioavailable iron input from shipboard aerosol sources to the ocean. *Global Biogeochem. Cycles* **27**, 1–10 (2013).
40. P. N. Sedwick, E. R. Sholkovitz, T. M. Church, Impact of anthropogenic combustion emissions on the fractional solubility of aerosol iron: Evidence from the Sargasso Sea. *Geochem. Geophys. Geosyst.* **8**, Q10Q06 (2007).
41. J. G. Acker, G. Leptoukh, Online analysis enhances use of NASA Earth science data. *Eos Trans. AGU* **88**, 14–17 (2007).
42. Z. Shi, M. D. Krom, S. Bonneville, A. R. Baker, T. D. Jickells, L. G. Benning, Formation of iron nanoparticles and increase in iron reactivity in mineral dust during simulated cloud processing. *Environ. Sci. Technol.* **43**, 6592–6596 (2009).
43. Z. Shi, Z. Shi, M. D. Krom, S. Bonneville, A. R. Baker, C. Bristow, N. Drake, G. Mann, K. Carslaw, J. B. McQuaid, T. Jickells, L. G. Benning, Influence of chemical weathering and aging of iron oxides on the potential iron solubility of Saharan dust during simulated atmospheric processing. *Global Biogeochem. Cycles* **25**, GB2010 (2011).
44. Z. Shi, S. Bonneville, M. D. Krom, K. S. Carslaw, T. D. Jickells, A. R. Baker, L. G. Benning, Iron dissolution kinetics of mineral dust at low pH during simulated atmospheric processing. *Atmos. Chem. Phys.* **11**, 995–1007 (2011).
45. K. V. Desboeufs, R. Losno, F. Vimeux, S. Cholbi, The pH-dependent dissolution of wind-transported Saharan dust. *J. Geophys. Res.* **104**, 21287–21299 (1999).
46. D. S. Mackie, P. W. Boyd, K. A. Hunter, G. H. McTainsh, Simulating the cloud processing of iron in Australian dust: pH and dust concentration. *Geophys. Res. Lett.* **32**, L06809 (2005).
47. G. Rubasinghege, R. W. Lentz, M. M. Scherer, V. H. Grassian, Simulated atmospheric processing of iron oxyhydroxide minerals at low pH: Roles of particle size and acid anion in iron dissolution. *Proc. Natl. Acad. Sci. U.S.A.* **107**, 6628–6633 (2010).
48. H. Fu, D. M. Cwiertny, G. R. Carmichael, M. M. Scherer, V. H. Grassian, Photoreductive dissolution of Fe-containing mineral dust particles in acidic media. *J. Geophys. Res.* **115**, D11304 (2010).
49. D. M. Cwiertny, J. Baltrusaitis, G. J. Hunter, A. Laskin, M. M. Scherer, V. H. Grassian, Characterization and acid-mobilization study of iron-containing mineral dust source materials. *J. Geophys. Res.* **113**, D05202 (2008).
50. L. J. Spokes, T. D. Jickells, B. Lim, Solubilisation of aerosol trace metals by cloud processing: A laboratory study. *Geochim. Cosmochim. Ac.* **58**, 3281–3287 (1994).
51. H. Chen, V. H. Grassian, Iron dissolution of dust source materials during simulated acidic processing: The effect of sulfuric, acetic, and oxalic acids. *Environ. Sci. Technol.* **47**, 10312–10321 (2013).
52. W. Li, L. Y. Shao, Transmission electron microscopy study of aerosol particles from the brown hazes in northern China. *J. Geophys. Res.* **114**, D09302 (2009).
53. W. Li, T. Wang, S. Zhou, S. C. Lee, Y. Huang, Y. Gao, W. Wang, Microscopic observation of metal-containing particles from Chinese continental outflow observed from a Non-industrial site. *Environ. Sci. Technol.* **47**, 9124–9131 (2013).
54. J. W. Chi, W. J. Li, D. Z. Zhang, J. C. Zhang, Y. T. Lin, X. J. Shen, J. Y. Sun, J. M. Chen, X. Y. Zhang, Y. M. Zhang, W. X. Wang, Sea salt aerosols as a reactive surface for inorganic and organic acidic gases in the Arctic troposphere. *Atmos. Chem. Phys.* **15**, 11341–11353 (2015).
55. W. Li, S. R. Chen, Y. S. Xu, X. C. Guo, Y. L. Sun, X. Y. Yang, Z. F. Wang, X. D. Zhao, J. M. Chen, W. X. Wang, Mixing state and sources of submicron regional background aerosols in the northern Qinghai–Tibet Plateau and the influence of biomass burning. *Atmos. Chem. Phys.* **15**, 13365–13376 (2015).
56. W. Li, Y. Wang, J. L. Collett Jr., J. Chen, X. Zhang, Z. Wang, W. Wang, Microscopic evaluation of trace metals in cloud droplets in an acid precipitation region. *Environ. Sci. Technol.* **47**, 4172–4180 (2013).
57. K. Li, B. Sinha, P. Hoppe, Speciation of nitrogen-bearing species using negative and positive secondary ion spectra with nano secondary ion mass spectrometry. *Anal. Chem.* **88**, 3281–3288 (2016).
58. C. Pöhlker, K. T. Wiedemann, B. Sinha, M. Shiraiwa, S. S. Gunthe, M. Smith, H. Su, P. Artaxo, Q. Chen, Y. Cheng, W. Elbert, M. K. Gilles, A. L. D. Kilcoyne, R. C. Moffet, M. Weigand, S. T. Martin, U. Pöschl, M. O. Andreae, Biogenic potassium salt particles as seeds for secondary organic aerosol in the Amazon. *Science* **337**, 1075–1078 (2012).
59. S. Ghosal, P. K. Weber, A. Laskin, Spatially resolved chemical imaging of individual atmospheric particles using nanoscale imaging mass spectrometry: Insight into particle origin and chemistry. *Anal. Methods* **6**, 2444–2451 (2014).

Acknowledgments: We thank B. Bloss from the University of Birmingham for his constructive comments to this paper. **Funding:** W.L. was funded by the National Natural Science Foundation of China (41575116 and 41622504) and Shandong Natural Science Funds for Distinguished Young Scholar (JQ201413). Z.S. acknowledges support by the U.K. Natural Environment Research Council (NE/I021616/1 and NE/K000845/1). A.N. acknowledges support from the Cullen-Peck Faculty Fellowship, the Georgia Power Faculty Scholar Chair, and the Johnson Faculty Fellowship. **Author contributions:** W.L. carried out TEM and AFM measurements; W.L. and Z.S. carried out data analysis and wrote the manuscript; L.X. prepared the samples in the laboratory; W.L., J.Z., and Y.L. carried out the NanoSIMS measurement; X.L., X.Y., P.F., and H.G. coordinated and ran the ship and conducted the aerosol sampling; D.Z. and L.S. contributed to data analysis and experimental measurement; J.C., W.W., X.Z., R.M.H., and A.N. contributed to data interpretation and manuscript drafting; and A.N. and Z.S. conceived the analysis procedure. All authors reviewed and commented on the paper. **Competing interests:** The authors declare that they have no competing interests. **Data and materials availability:** All data needed to evaluate the conclusions in the paper are present in the paper and/or the Supplementary Materials. Additional data related to this paper may be requested from the authors.

Submitted 27 July 2016
Accepted 31 January 2017
Published 1 March 2017
10.1126/sciadv.1601749

Citation: W. Li, L. Xu, X. Liu, J. Zhang, Y. Lin, X. Yao, H. Gao, D. Zhang, J. Chen, W. Wang, R. M. Harrison, X. Zhang, L. Shao, P. Fu, A. Nenes, Z. Shi, Air pollution–aerosol interactions produce more bioavailable iron for ocean ecosystems. *Sci. Adv.* **3**, e1601749 (2017).

Science Advances

Air pollution–aerosol interactions produce more bioavailable iron for ocean ecosystems

Weijun Li, Liang Xu, Xiaohuan Liu, Jianchao Zhang, Yangting Lin, Xiaohong Yao, Huiwang Gao, Daizhou Zhang, Jianmin Chen, Wenxing Wang, Roy M. Harrison, Xiaoye Zhang, Longyi Shao, Pingqing Fu, Athanasios Nenes and Zongbo Shi

Sci Adv **3** (3), e1601749.
DOI: 10.1126/sciadv.1601749